Neuroscience 256 (2014) 412–425

QUANTIFICATION OF THE DENSITY OF COOPERATIVE NEIGHBORING SYNAPSES REQUIRED TO EVOKE ENDOCANNABINOID SIGNALING

B. PACHOUD,[a] P. SHARMA,[a] A. BERGEROT,[a] T. KNÖPFEL[c] AND P. MARCAGGI[a,b]*

[a] *Department of Neuroscience, Physiology and Pharmacology, University College London, Gower Street, London WC1E 6BT, UK*

[b] *IBENS, INSERM U1024 CNRS UMR8197, Ecole Normale Supérieure 46, rue d'Ulm, 75005 Paris, France*

[c] *Division of Brain Sciences, Imperial College, London, Hammersmith Hospital, Du Cane Road, London W12 0NN, UK*

Abstract—The spatial pattern of synapse activation may impact on synaptic plasticity. This applies to the synaptically-evoked endocannabinoid-mediated short-term depression at the parallel fiber (PF) to Purkinje cell synapse, the occurrence of which requires close proximity between the activated synapses. Here, we determine quantitatively this required proximity, helped by the geometrical organization of the cerebellar molecular layer. Transgenic mice expressing a calcium indicator selectively in granule cells enabled the imaging of action potential-evoked presynaptic calcium rise in isolated, single PFs. This measurement was used to derive the number of PFs activated within a beam of PFs stimulated in the molecular layer, from which the density of activated PFs (input density) was calculated. This density was on average 2.8 μm^{-2} in sagittal slices and twice more in transverse slices. The synaptically-evoked endocannabinoid-mediated suppression of excitation (SSE) evoked by ten stimuli at 200 Hz was determined from the monitoring of either postsynaptic responses or presynaptic calcium rise. The SSE was significantly larger when recorded in transverse slices, where the input density is larger. The exponential description of the SSE plotted as a function of the input density suggests that the SSE is half reduced when the input density decreases from 6 to 2 μm^{-2}. We conclude that, although all PFs are truncated in an acute sagittal slice, half of them remain respondent to stimulation, and activated synapses need to be closer than 1.5 µm to synergize in endocannabinoid signaling.

Key words: cerebellum, synaptic plasticity, brain slice, cannabinoids, calcium imaging.

INTRODUCTION

Endocannabinoids modulate synaptic transmission by signaling in a direction opposite to information transfer (retrograde) and by depressing neurotransmitter release (Chevaleyre et al., 2006; Kano et al., 2009). Two types of mechanisms have been shown to trigger this retrograde signaling. First, depolarization of the postsynaptic neuron induces endocannabinoid release which mediates the so-called depolarization-induced suppression of excitation (DSE) or inhibition (DSI) by activation of cannabinoid receptors CB1 expressed on excitatory or inhibitory terminals respectively (Llano et al., 1991a; Kreitzer and Regehr, 2001; Ohno-Shosaku et al., 2001). It remains unclear whether the long (few seconds) experimental injection of depolarizing currents into the postsynaptic neuron, required to evoke DSE or DSI, has physiological correlates. Second, repetitive activation of excitatory synapses at high frequency leads to postsynaptic metabotropic glutamate receptors activation and depolarization, the combination of which induces endocannabinoid release and the depression of excitatory or inhibitory afferents, called synaptically-induced suppression of excitation (SSE) or synaptically-induced suppression of inhibition, respectively (Safo et al., 2006; Heifets and Castillo, 2009). In contrast to DSE and DSI, SSE is evoked by synaptic activity, and hence may be considered as physiologically more relevant.

Furthermore, in contrast to DSE or DSI, SSE has been proposed to be input specific, i.e. only the input that has triggered the endocannabinoid release is depressed (Brown et al., 2003). This conclusion is based on the comparison of the stimulation of separate clusters of hundreds of excitatory synapses in close proximity. So the input specificity of SSE has been resolved at a scale far larger than the distance between neighboring synapses (Brown et al., 2003). If the SSE was *synapse-specific* (i.e. occurring at individual activated synapses, but not their neighbors) it might

*Correspondence to: P. Marcaggi, IBENS, INSERM U1024 CNRS UMR8197, Ecole Normale Supérieure 46, rue d'Ulm, 75005 Paris, France. Tel: +33-144323751.
E-mail address: paikan.marcaggi@ens.fr (P. Marcaggi).

Abbreviations: 4-AP, 4-aminopyridine; CV, coefficient of variation; DSE, depolarization-induced suppression of excitation; DSI, depolarization-induced suppression of inhibition; EGTA, ethylene glycol tetraacetic acid; fEPSP, field excitatory post-synaptic potential; FV, fiber volley; GL, granular layer; HEPES, 4-(2-hydroxyethyl) piperazine-1-ethanesulfonic acid; LED, light-emitting diode; ML, molecular layer; PF, parallel fiber; SSE, synaptically-induced suppression of excitation.

0306-4522
http://dx.doi.org/10.1016/j.neuroscience.2013.10.041

have been expected to be inducible independently of the spatial pattern of the input. However, at cerebellar PF synapses, we showed that the SSE is only detected when the cooperation between neighboring synapses is enhanced, as occurs for spatially clustered activated synapses, i.e. high input density (Marcaggi and Attwell, 2005, 2007).

The required input density remains to be quantified. It could be that the input density does not need to be high, as long as a number of inputs converge onto the same dendritic area to enable the summation of postsynaptic events upstream the endocannabinoid release. Alternatively, very high input density might be required for the enhancement of glutamate spillover effects, which determine endocannabinoid release (Marcaggi and Attwell, 2005). Here, we report a quantitative description of PF input density in acute slices and how SSE depends on it.

The input density predicted from anatomical studies is likely to differ in acute slices due to limited tissue preservation following slicing procedures. We devised a method to determine the density of PFs which exhibit $[Ca^{2+}]_i$ rise in response to stimulation. The density was found to be highly variable, with an average value of 2.8 μm^{-2} in sagittal slices and twice more in transverse slices. The SSE dependence on slice orientation and the plot of the SSE against the extended range of input densities obtained by pooling data from sagittal and transverse slices suggest that the SSE requires input densities close to the anatomical maximum to occur.

EXPERIMENTAL PROCEDURES

Ethics statement

In accordance with the United Kingdom Animal (Scientific Procedures) Act of 1986, this study was covered by the Home Office project license PPL 70/05771 for the breeding GCaMP2 (transgenic) mice. Mice were humanely killed at a designated establishment by cervical dislocation, which is an appropriate method under Schedule 1 of the Act.

Animals

We used ICR transgenic mice expressing the fluorescent calcium indicator protein GCaMP2 under the control of regulatory sequences of the gene coding Kv3.1 potassium channel which, in the cerebellum, is selectively expressed in granule cells (Diez-Garcia et al., 2005). P10–P15 mice were used and were decapitated following cervical dislocation. The brain was swiftly extracted and immersed in ice cold incubation medium.

Solutions

The incubation solution was composed of (mM): 120 NaCl, 2.5 KCl, 1 NaH_2PO_4, 26 $NaHCO_3$, 2 $CaCl_2$, 1 $MgCl_2$, 25 glucose, 4 pyruvate and 1 kynurenic acid (to block glutamate receptors), equilibrated with 95% O_2/5% CO_2. The perfusion solution was composed of the same except no kynurenic acid or pyruvate was present, the $CaCl_2$ concentration was 3 mM and 10 μM GABAzine was added to block $GABA_A$ receptors. For all the experiments, unless otherwise stated, the slicing solution was named "High Potassium Slicing Medium" and was composed of (mM): 130 K-gluconate, 15 KCl, 0.05 EGTA, 20 HEPES, 25 glucose, 3 kynurenic acid and 4 pyruvate with pH adjusted to 7.4 with NaOH and osmotic pressure equated to 300 mOsm (Dugue et al., 2005).

Cerebellar slices

The cerebellum was dissected and glued on agar with tissue adhesive (3 M, Vetbond). Horizontal (300-μm thick) or vermis sagittal (250-μm thick) slices were cut in < 4 °C slicing medium with a VT1200S slicer (Leica) with vibration at 85 Hz of 1.40 mm amplitude and forward movement of 0.05 mm s^{-1} speed. Slices were then transferred into an incubation medium at 4 °C for 2 min, at room temperature for 20 min, at 35 °C for 20 min and then at room temperature (24 ± 1 °C) for up to 8 h. Since our study addresses how the slice quality affects endocannabinoid signaling, we have tried a range of slicing parameters until we obtained recordings with the most reliable SSE. We have compared our slicing medium to the one used in the reports on endocannabinoid signaling at PF synapses from Regehr and coll., which we named "High Sucrose Slicing Medium" and was composed of (mM): 81.2 NaCl, 23.4 $NaHCO_3$, 69.9 sucrose, 23.3 glucose, 2.4 KCl, 1.4 NaH_2PO_4, 6.7 $MgCl_2$, and 0.5 $CaCl_2$ bubbled with 95% O_2/5% CO_2 and osmotic pressure equated to 300 mOsm. Interleaved experiments were performed for horizontal slices obtained with each slicing medium. SSE was significantly more potent for slices obtained with the High Potassium Slicing Medium (42.8 ± 4.88%, n = 18) than for slices obtained with the High Sucrose Slicing Medium (25.7 ± 3.07%, n = 24; p = 0.003). However, the input density, shown below to correlate with the potency of SSE, was not affected by the nature of the slicing medium. We do not have an explanation for why slices obtained with the High Potassium Slicing Medium showed a more potent SSE.

Recording

Slices were placed in a chamber under an upright microscope (BX51; Olympus) and superfused at a rate of 2 ml min^{-1}. Pipettes were pulled from borosilicate glass capillaries with filament of 1.5-mm outer diameter and 1.17-mm inner diameter (Harvard Apparatus) and filled with perfusion solution for field stimulation and recording. Stimulation electrodes had tips of 3–4 μm diameter (1–2 MΩ) and were positioned in the molecular layer, on the surface of upper face of the sagittal slice. Recording electrodes of 2–3 MΩ were positioned 75 μm vertically below the stimulating electrode. For transverse slices, stimulating and recording electrodes were positioned on the same horizontal plane, about 30 μm below the surface and about 75 μm from each other. Molecular layer stimulation was typically a negative square pulse of 20 V × 100 μs (except in Fig. 3 where

stimulation intensity was varied as stated in the figure legend). Extracellular field potentials were recorded using a Multiclamp 700B amplifier and digitized by a Digidata 1440A (Molecular Devices, USA). The field potential was composed of a fiber volley (measured as its negative peak, FV) followed by a field excitatory post-synaptic potential (measured as its negative peak, fEPSP, or as its integrated value over time, $fEPSP_{int}$). The SSE amplitude was calculated as the percentage reduction of the fEPSP (or the $fEPSP_{int}$ – see figure legend) at +8 s following the induction burst, relative the averaged baseline value measured for the 2 min preceding the burst.

Image acquisition

A back illuminated cooled charge-coupled device camera (Andor iXon) was used to capture images with Andor IQ 1.8 software (Andor Technology, Belfast, UK). Olympus water immersion objective ×40, N.A. 0.8 (Fig. 1) and ×60, N.A. 0.9 (Figs. 2 and 3) were used. A blue light-emitting diode (LED) (Cairn Research, UK) provided excitation at 468 nm. Emission above 500 nm was collected through a beam splitter and a 500–540 nm band pass filter (Chroma). PFs were repetitively (0.25 Hz) stimulated at the tip of the stimulating electrode by two 50 ms apart 100-μs pulses of 10–30 V. In synchrony with this repeat, two images were captured using 50-ms exposure time: the first image was captured 2 s prior the stimulation (baseline image). The second image (response image) was captured 125 ms after the first stimulating pulse to be in phase with the peak of the GCaMP2 fluorescence change (Diez-Garcia et al., 2005). The EM gain of the camera improved the signal-to-noise by about a factor of 3. We carefully checked that the EM gain did not significantly affect the linear summation of fluorescent signals in the range of the fluorescence intensity measured from slices. This linearity was verified by calibration, using a FocalCheck

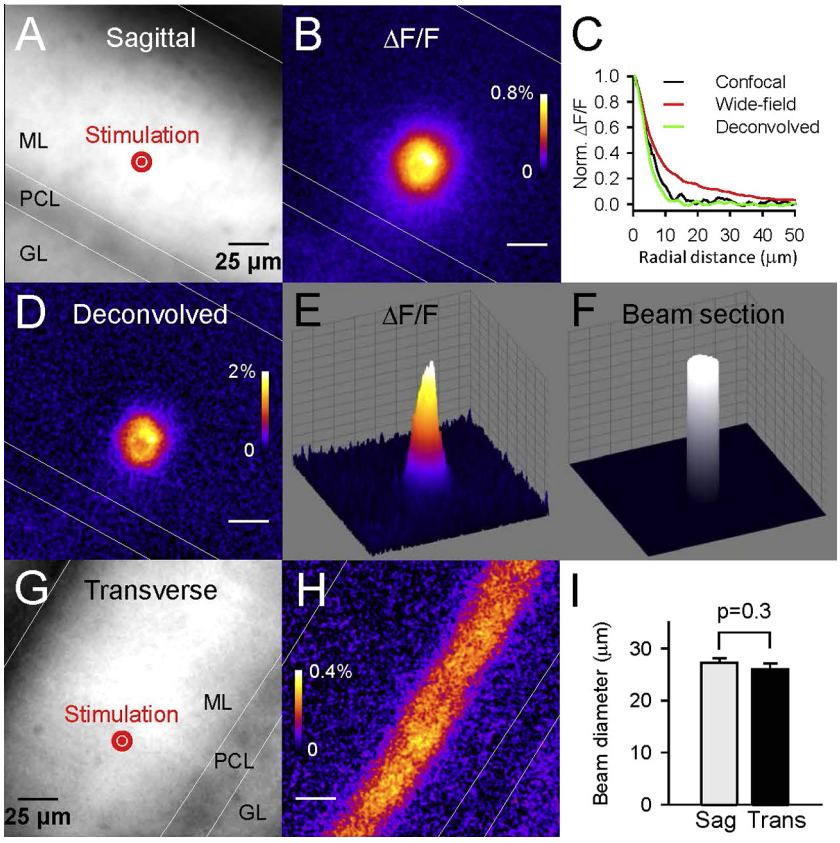

Fig. 1. Beams of activated PFs in sagittal and transverse slices, imaged from the detected change in $[Ca^{2+}]_i$. (A) Fluorescence image from a sagittal slice from a GCaMP2 mouse. The molecular layer (ML) exhibits more fluorescence than the granular layer (GL) and the Purkinje cell layer (PCL). The site of stimulation with a monopolar electrode is shown in red. (B) $\Delta F/F$ image of the same slice showing the transient change of GCaMP2 fluorescence (indicating a transient $[Ca^{2+}]_i$ rise) following double-pulse stimulation. (C) Radial profile of $\Delta F/F$ signal from a beam of activated PFs obtained with wide field fluorescence microscopy (red line) or with confocal microscopy (black line). Deconvolution (see "Experimental procedure") of the signal obtained with epifluorescence microscopy provided a $\Delta F/F$ signal (green line) with a radial profile similar to the signal obtained with confocal microscopy. (D) Same $\Delta F/F$ image as in (B), deconvolved. (E) 3D representation of the $\Delta F/F$ signal shown in (D). (F) 3D representation of the $\Delta F/F$ integrated area ($\Delta F/F$ integrated over the sagittal plane and divided by $\Delta F/F$ maximum) calculated for image in (D, E). The integrated area was used to define the section of the beam of activated PFs (see "Experimental procedure"). (G) Fluorescence image from a transverse slice from a GCaMP2 mouse. (H) $\Delta F/F$ image of the same slice showing the transient change of GCaMP2 fluorescence following double-pulse stimulation at the site indicated in (G). (I) Averaged diameter of the beam sections for stimulations in sagittal slices (Sag, $n = 41$) or in transverse slices (Trans, $n = 25$). (For interpretation of the references to color in this figure legend, the reader is referred to the web version of this article.)

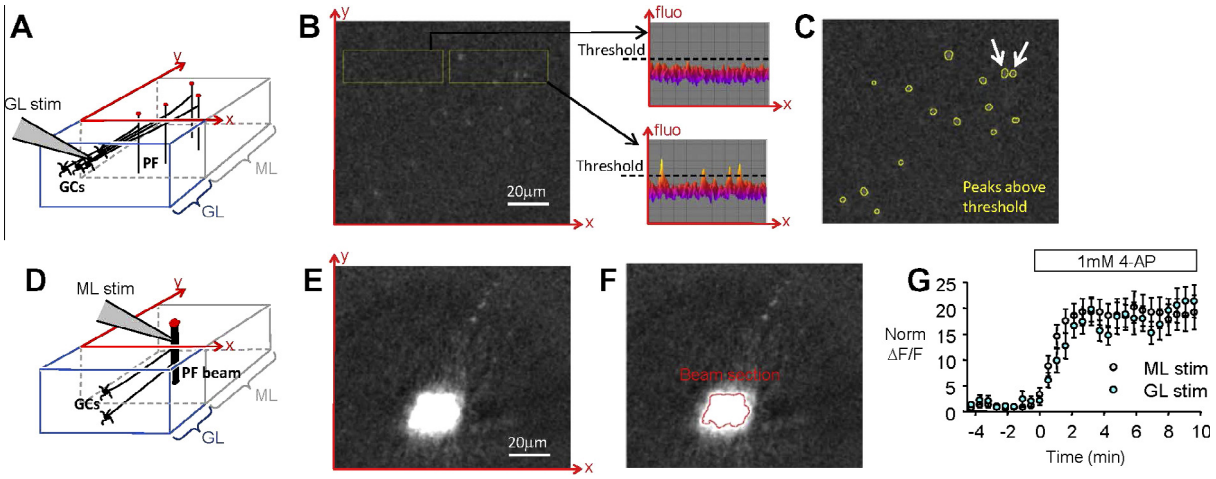

Fig. 2. Imaging of isolated activated PFs from sagittal slices. (A) Schematic 3D diagram showing the predicted effect of stimulating in the granular layer (GL). The scheme shows a block of cerebellar cortex in a sagittal slice including portions of ML and GL. The (x, y) plane is the plane of the $\Delta F/F$ image of the ML. Activated PFs crossing the horizontal (x, y) plane are expected to be vertical, and hence detected as dots in the $\Delta F/F$ image (red dots). (B) $\Delta F/F$ image from the ML of a slice where stimulation was in the adjacent GL (not in the field of view). Slice was superfused with 1 mM 4-AP. Peaks of $\Delta F/F$ arising from isolated PFs are detected above the noise level, as illustrated by the two insets showing 3D representation of $\Delta F/F$ over ROIs displayed with yellow squares. (C) Isolated $\Delta F/F$ peaks were selected to determine the averaged integrated $\Delta F/F$ signal arising from them (see Fig. 3D). Insufficiently isolated $\Delta F/F$ peaks (arrows) were ignored. (D) Schematic 3D diagram showing the effect of stimulating in the molecular layer (ML). (E) $\Delta F/F$ image from the same ML region shown in (B) but obtained for stimulation in the ML. The integrated $\Delta F/F$ signal arising from the stimulated PF beam was calculated from a large area covering the beam. (F) The beam section (see ''Experimental procedure'' for calculation) is shown as the red contour. (G), The $\Delta F/F$ signals were amplified by 4-AP, the effect of which was similar for $\Delta F/F$ signals evoked by ML or GL stimulation. The enhancement produced by 4-AP remained stable for at least 10 min. Black and white $\Delta F/F$ images have same contrast setting running from −0.96% to 7.40%. (For interpretation of the references to color in this figure legend, the reader is referred to the web version of this article.)

fluorescent microscope test slide containing beads with defined fluorescent intensities (Invitrogen).

$\Delta F/F$ measurement

ImageJ was used for most image analysis. The change in GCaMP2 fluorescence ($\Delta F/F$) evoked by PF stimulation was determined from the difference between the response and the baseline images, divided by the baseline value. The slight bleaching (0.028 + 0.009% per frame, n = 32) was systematically measured (over parts of the image where the stimulation had no detectable effect) and taken into account in the $\Delta F/F$ calculation. The $\Delta F/F$ value refers to the mean over all pixels within a region of interest (the beam section, as described below). The $\Delta F/F$ image revealed the shape of the bundle of stimulated PFs, which appeared as a disk for sagittal slices (Fig. 1B) or as a beam following the anatomical course of PFs for transverse slices (Fig. 1H). Images shown in Figs. 1–3 represent the average of multiple trials (up to ∼150). The use of 4-AP (see text) and the deconvolution amplified the $\Delta F/F$ values by ∼20 times (Fig. 2E) and ∼2 times respectively, overall amplifying the $\Delta F/F$ signals ∼40 times (Figs. 2 and 3).

Determination of the beam section

The beam section refers to the area covered by imaged activated PFs in a slice perpendicular to the direction of PFs (sagittal slice). The boundaries of this area are expected to be diffuse as the probability of a PF to be activated by the stimulation will gradually decrease with the distance from the stimulating electrode. However, part of the diffuse aspect of the boundaries of the $\Delta F/F$ signal (Fig. 1B) reflected light scattering and diffusion from non-focal planes, as demonstrated by the sharper edge obtained by confocal microscopy (Fig. 1C). This light scattering was corrected for by deconvolution using ImageJ plugins Diffraction_PSF_3D and Iterative_Deconvolution (http://www.optinav.com) (Fig. 1B–D). Longitudinal spherical aberration of 10 µm and low-pass circle diameter of 1 pixel were used in order to transform images obtained by epifluorescence into images similar to the ones obtained by confocal microscopy (Fig. 1C). We checked that the deconvolution did not affect the ratio of the integrated $\Delta F/F$ measured over activated PF beams and over isolated PFs (p = 0.874, five experiments). So, deconvolved images could be used to quantify the number of activated PFs in stimulated beams by the method detailed below. For sagittal slices, the beam section was defined as the ''integrated area'' of $\Delta F/F$, i.e. the area that would be occupied by a beam with a homogenous $\Delta F/F$ (equaled to the peak $\Delta F/F$ of the real $\Delta F/F$ image) over its section and producing the same integrated $\Delta F/F$ (Fig. 1F). The peak $\Delta F/F$ was determined from radial plots centered on the centroid of the $\Delta F/F$ response. Most beam sections were round with radial symmetry (Figs. 1D and 3A). The diameter of the beam was calculated based on a disk having the area of the beam section. Similarly, for transverse slices

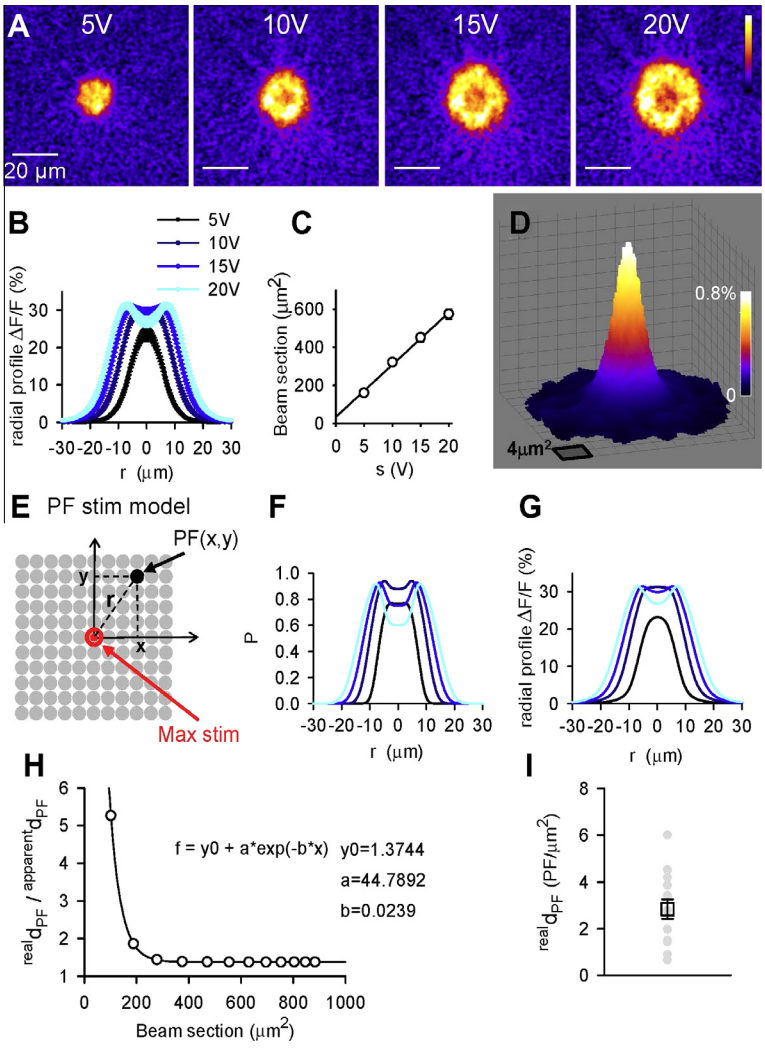

Fig. 3. Determination of the density of PFs which exhibit a $[Ca^{2+}]_i$ rise when stimulated ($^{real}d_{PF}$). (A) $\Delta F/F$ images of activated PFs stimulated with increasing intensities (5, 10, 15 and 20 V × 100 µs), showing increasing PF beam sections and increasing drop of fluorescence change in the center of the beam. (B) Averaged radial profiles of $\Delta F/F$ signals for beams stimulated as in (A) (n = 20). (C) Averaged beam sections (integrated areas of $\Delta F/F$ signals, see ''Experimental procedure'') plotted against the stimulation intensities, showing a clear linear correlation (n = 20). (D) Averaged $\Delta F/F$ signal produced by isolated activated PFs (as in Fig. 2B) (n = 83). Most of the 83 signals were asymmetrical (presumably because PFs were not perfectly perpendicular to the plane of the slice). They were averaged after having been centered to the pixel of highest intensity. This averaging led to an area of fluorescence change much larger than that expected from a single PF (1 pixel is 0.267 µm^2). Part of this spatial spread may also result from imperfect deconvolution. (E) Schematic diagram of the model of PF activation by stimulation in the ML (PF stim model). The model postulates that, in a sagittal slice, PFs are perpendicular to the imaged plane and defined by two coordinates (x, y) in this plane; PFs are homogeneously distributed across the ML with a constant density $^{real}d_{PF}$ (parameter implemented in the model); PFs have all the same excitability threshold. (F, G) Simulated radial profiles of the probability P (derived from Eq. (4)) of activating a PF (F) and $\Delta F/F$ signals corresponding to this spatial distribution of P (G). Parameter of the PF stim model (s_{act}, s_{kill}, E_{act} and E_{kill}) were determined from the best fit of the experimental $\Delta F/F$ radial profiles shown in (B), obtained for stimulation intensities 5, 10, 15 and 20 V. (H) Relationship between the apparent PF density ($^{apparent}d_{PF}$) and $^{real}d_{PF}$. $^{apparent}d_{PF}$ and the beam section were calculated from simulated $\Delta F/F$ responses as they would have been from experimental responses (see ''Results''). The plot shows that $^{apparent}d$ is an underestimate of $^{real}d_{PF}$ and $\alpha = {}^{real}d_{PF}/{}^{apparent}d_{PF}$ provides a correction factor to calculate $^{real}d_{PF}$ from $^{apparent}d_{PF}$ calculated experimentally. (I) Calculated $^{real}d_{PF}$ from $^{apparent}d_{PF}$ experimentally determined for 11 experiments as the one shown in Fig. 2B, E. (For interpretation of the references to color in this figure legend, the reader is referred to the web version of this article.)

(Fig. 1H), the diameter of the beam was derived from the integrated area of $\Delta F/F$ measured over a wide rectangular ROI covering the activated PF beam and parallel to it.

Modeling

As defined in the ''Result'' section (Eq. (4)), the probability P that a PF located at the tip of the stimulating electrode gets activated is $P = A_0 \times (1 - K_0)$, where A_0 is the probability that the PF is depolarized enough to generate an action potential and K_0 is the probability that the PF is destroyed by the stimulation. These probabilities were set to follow simple Gaussian dependence on the stimulation intensity s: $A_0 = 1 - \exp(-s^2/s_{act}^2)$ and $K_0 = 1 - \exp(-s^2/s_{kill}^2)$, where s_{act} and s_{kill} ($s_{act} < s_{kill}$) are determined by fitting experimental data (see below). The probability P that a PF located at a distance $r > 0$ from

the tip of the stimulating electrode gets activated is $P = A_0 \times A \times (1 - K_0 \times K)$, where $A_0 \times A$ is the probability that the PF is depolarized enough to generate an action potential and $K_0 \times K$ is the probability that the PF is destroyed by the stimulation. A and K follow simple Gaussian dependence on the electrostatic field E for $r > 0$ (Eq. (3)): $A = \exp(-E_{act}^2/E^2)$ and $K = \exp(-E_{kill}^2/E^2)$. Iterative simulations provided $\Delta F/F$ profiles whose best fits of experimental data were obtained for $s_{act} = 4$ V, $s_{kill} = 28$ V, $E_{act} = 75$ GV m^{-1} and $E_{kill} = 500$ GV m^{-1}.

The signal produced at coordinate (x, y) by an activated PF located at (x_0, y_0) was defined by

$$\Delta F/F(x,y) = (a/(1 + ((x - x_0)^2 + (y - y_0)^2)/b^2)) \times exp(-0.5 \times ((x - x_0)^2 + (y - y_0)^2)/c^2) \quad (1)$$

where a, b and c were obtained from the best empirical fit of the experimental $\Delta F/F$ image averaged from 83 single isolated PFs (Fig. 3D; $a = 2.376$, $b = 0.813$ µm and $c = 13.3$ µm).

Data analysis

Data are presented as mean ± SEM, unless otherwise stated. Significance was determined by two-tailed t-test. Spearman rank order correlation was used to assess the significance of the correlation between the parameters of synaptic transmission (Fig. 7). For all experiments, the N number refers to the number of used slices.

RESULTS

Imaging beams of activated parallel fibers

The length of PFs (2 mm in mice, 4 mm in rat) (Pichitpornchai et al., 1994; Soha et al., 1997) enables their selective loading with dyes (in transverse slices, where PFs are in the plane of the slice) following local bulk loading away from the site of interest and diffusion of the loaded dyes along the PF cytoplasm. This method has been extensively used with fluorescent calcium indicators to investigate volume-averaged calcium concentration changes in PFs ($\Delta[Ca^{2+}]_{PF}$) (Mintz et al., 1995; Beierlein et al., 2004; Daniel et al., 2004), which mainly reflect presynaptic calcium changes because most cytoplasmic volume in PF is contained by presynaptic boutons (Palay and Chan-Palay, 1974; Xu-Friedman et al., 2001). The monitoring $\Delta[Ca^{2+}]_{PF}$ was equally achieved from transverse cerebellar slices of mice expressing the calcium indicator GCaMP2 in granule cells and their axons (Diez-Garcia et al., 2005). Here, we used these mice to monitor $\Delta[Ca^{2+}]_{PF}$ in sagittal slices, where PFs run perpendicular to the plane of the slice. PF stimulation in the molecular layer (ML; Fig. 1A) was followed by a transient change in GCaMP2 fluorescence ($\Delta F/F$; Fig. 1B). The signal showed a remarkable radial symmetry (Fig. 1B) as expected from a PF beam being perpendicular to the plane of the slice and PF excitability being homogenous within the molecular layer. The edge of the $\Delta F/F$ signal was less sharp than the one obtained by confocal imaging (Fig. 1C) indicating that the light dispersion occurring with epifluorescence imaging contributed to this blurred edge. This effect of light dispersion was corrected by deconvolution (Fig. 1C–E; see "Experimental procedure"). After correction, the gradual decrease of $\Delta F/F$ at the edge of the beam was considered to mostly reflect gradual decrease in the density of activated PFs. The beam section could be assimilated to a disk from which the beam diameter was calculated (see "Experimental procedure"). When PF beams were stimulated with similar intensities in sagittal or transverse slices, their diameters were not significantly different ($p = 0.35$; Fig. 1I), indicating that PF excitability was unaffected by the slice orientation.

Apparent density of PFs responding to ML stimulation

The number N of PFs activated by molecular layer stimulation and imaged as a beam is given by:

$$N = \left(\int_{xy} \Delta F/F\right)_{beam} / \left(\int_{xy} \Delta F/F\right)_{1PF} \quad (2)$$

where $(\int_{xy}\Delta F/F)_{beam}$ and $(\int_{xy}\Delta F/F)_{1PF}$ are the integrated $\Delta F/F$ over the sagittal plane measured for the stimulation of the PF beam and the stimulation of a single PF, respectively. This formula applies provided the images of the activated beam and the image of the isolated activated PF are obtained for the same focal plane, and the fluorescence signals summate linearly over the investigated range (see "Experimental procedure"). To determine $(\int_{xy}\Delta F/F)_{1PF}$, we imaged PF activation when stimulating in the granular layer, a configuration expected to result in the activation of parallel fibers spatially separated from each over (Fig. 2A) (Marcaggi and Attwell, 2005). In order to increase the signal to noise of $\Delta F/F$ measurements, slices were superfused with the potassium channel blocker 4-aminopyridine (4-AP, 1 mM) which has been reported to amplify the peak and the duration of action potential-evoked calcium changes in PFs (Daniel and Crepel, 2001; Brown et al., 2004). 4-AP amplified the PF calcium change evoked by stimulation in the molecular layer or in the granular layer by similar amounts (by 18.7 and 17.6 times respectively, $p = 0.74$, $n = 10$; Fig. 2G). For granular layer stimulation, small isolated peaks of $\Delta F/F$ were clearly identified above the noise level in the molecular layer (Fig. 2B). These isolated peaks were identified as individual or small clusters of PFs. For the experiment illustrated in Fig. 2B–F, the average $(\int_{xy}\Delta F/F)_{1PF}$ was 76%·pixel, while $(\int_{xy}\Delta F/F)_{beam}$ was 70317%·pixel. We deduce from these two values, using Eq. (1), that N was 929, i.e. 929 PF were activated by the molecular layer stimulation shown in Fig. 2E. The apparent density of PFs ($^{apparent}d_{PF}$) is given by

$$^{apparent}d_{PF} = N/S_{beam} \quad (3)$$

where S_{beam} is the beam section (see Fig. 1F and "Experimental procedure"). In the example shown in Fig. 2B–F, S_{beam} was 323 µm^2, thus $^{apparent}d_{PF}$ was 2.9 PF µm^{-2}.

Modeling of PF activation in a sagittal slice

The density of activated PFs is not expected to be homogenous over the PF beam section. While most PFs may respond to the stimulation in the vicinity of the stimulating electrode, further away, the fraction of activated PFs will decrease continuously with the distance. In addition, only a fraction of PFs may get recruited for low-stimulation intensity while high-stimulation intensity may damage PFs in the center of the beam as suggested by images obtained for increased stimulation intensity (Fig. 3A and B; for high-stimulation intensity, the decreased $\Delta F/F$ signal in the center of the beam overlaps with a steady increase in baseline GCaMP2 fluorescence, further supporting the damage of PFs). Thus, the density of activated PFs is actually non-homogenous. We have modeled this non-homogeneity in order to derive the density of PFs which are preserved in an acute slice and can produce detectable calcium responses to stimulation ($^{real}d_{PF}$) from the first approximation $^{apparent}d_{PF}$ obtained from the imaging of the non-homogenous activated PFs.

In the model, we assumed that the anatomical PF distribution was homogenous throughout the molecular layer and PFs were identified by their location in the sagittal plane relative to the site of stimulation (Fig. 3E). The activation of one PF was set to produce a $\Delta F/F$ signal identical to the average of $\Delta F/F$ responses obtained from 83 isolated PF signals (Fig. 3D; from 15 experiments similar to the one illustrated in Fig. 2B, D). The probability P that a PF at coordinates (x, y) gets activated depended on the stimulation intensity and its distance r from the stimulating electrode. P was defined as follows.

According to Gauss' law, a PF at a distance r from the unipolar stimulating electrode tip, is exposed to an electric field

$$E = (s \times \Delta t/R)/4\pi\varepsilon_0 r^2 \quad (4)$$

where s is the voltage pulse (in V); Δt, its duration (in s), R, the resistance of the stimulating electrode (in Ω); ε_0, the electric constant (in $C\,V^{-1}m^{-1}$). We assumed that the activation (triggering an action potential) of PFs is determined by the intensity of E, which must be over a threshold E_{min}. It follows that the size of the stimulated beam, for a stimulation intensity s is given by the value r_{max} of r calculated from Eq. (3) with $E = E_{min}$. Eq. (3) predicts that the beam section (proportional to r^2_{max}) will increase linearly with the stimulation intensity. Consistently, our experimental measurement of the beam section obtained for 5, 10, 15 and 20 V stimulations exhibits a clear linearity when plotted against the stimulation intensity (Fig. 3C, $n = 20$).

To model the spatial distribution of PF activation, we defined the probability P that a PF at a distance r from the stimulating electrode responds to the stimulation as follows.

$$P = A_0 \times A \times (1 - K_0 \times K) \quad (5)$$

A_0 is the probability that a PF in the center of the beam ($r = 0$) gets activated (or killed, due to excessive electroporation). K_0 is the probability that a PF in the center of the beam ($r = 0$) gets killed. A is the probability that a PF, which would have responded in the center of the beam, responds at a distance r. K is the probability that a PF which would have been killed in the center of the beam, gets killed at a distance r. A_0, K_0, A and K were defined as Gaussian functions of the stimulation intensity (see "Experimental procedure") whose parameters were determined by iterative simulations until obtaining radial profiles (Fig. 3G) similar to ones obtained experimentally (Fig. 3B). The radial profile of P (Fig. 3F) is not identical to the radial profile of $\Delta F/F$ (Fig. 3G), due to the width of $\Delta F/F$ responses of individual PFs (Fig. 3D) producing spatial summation between neighboring $\Delta F/F$ responses. The amplitude of the radial profiles was determined by the value of $^{real}d_{PF}$ implemented in the model.

Preserved PFs in acute slices, real PF density

Simulations were obtained for increasing stimulation intensities and were used to calculate $^{apparent}d_{PF}$ from simulated $\Delta F/F$ signals (using Eqs. (1) and (2)). The values of $^{apparent}d_{PF}$ were systematically smaller than the values of $^{real}d_{PF}$ implemented in the model as shown by $\alpha = {}^{real}d_{PF}/{}^{apparent}d_{PF}$ plotted against the beam section (Fig. 3H). The factor α did not significantly vary for variations of the implemented $^{real}d_{PF}$ in the range [0.1–10] (not shown) but varied with the beam section (Fig. 3H). Eleven experiments as the one illustrated in Fig. 2B, D were used to convert $^{apparent}d_{PF}$ into $^{real}d_{PF}$, by using the value of α corresponding to the measured beam section. The $^{real}d_{PF}$ values showed a large variation with an average of $2.8 \pm 1.6\ \mu m^{-2}$ ($\pm$SD, $n = 11$; Fig. 3I).

Synaptically-evoked suppression of excitation (SSE) monitored from extracellular recordings and presynaptic $[Ca^{2+}]_i$ imaging

The input density is known to impact on the induction of plasticity *in vitro* (Marcaggi and Attwell, 2005, 2007), albeit qualitatively since the density of preserved PFs in acute slices has been unknown. In this second part of the study, we are re-assessing the dependency of endocannabinoid signaling on input density in light of the quantification of $^{real}d_{PF}$. The ability of Purkinje cells to release endocannabinoids following a burst of PF stimulation has been extensively investigated by patch-clamp experiments in whole-cell configuration (Brown et al., 2003; Beierlein et al., 2004; Marcaggi and Attwell, 2005; Safo and Regehr, 2005; Tanimura et al., 2010). Here, we monitored PF to Purkinje cell synaptic transmission extracellularly. This technique is less invasive (PCs cytoplasm remains intact) and enables the monitoring of the PF volley (FV) which reflects the action potential propagation along PFs (Fig. 4A; Bergerot et al., 2013), and provides a mean to calculate an index of input density (see below). Most of the fEPSP accounted for excitatory transmission as it was reduced by 97 ± 2% in NBQX 10 μM ($n = 5$; $p = 10^{-6}$). It has been estimated that about 94% of parallel fiber boutons contact Purkinje cells (Palkovits et al., 1971; Palay and

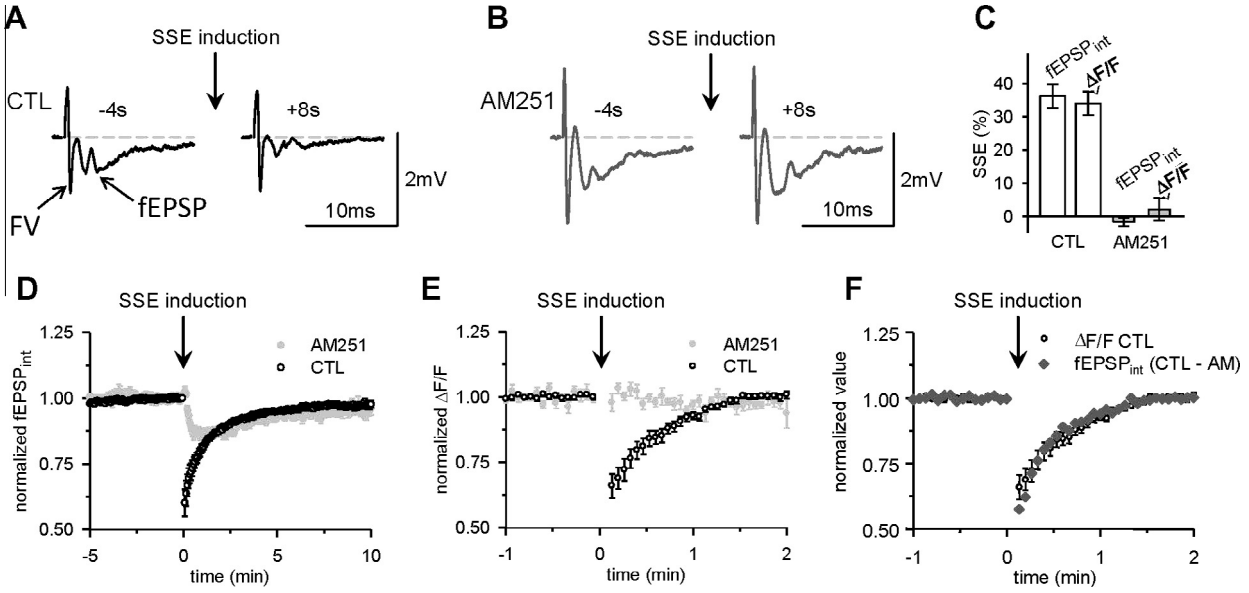

Fig. 4. Monitoring of synaptically-evoked endocannabinoid signaling. (A) Specimen trace showing the local field potential recorded in the molecular layer following PF stimulation. The local field potential comprises a fiber volley (FV) reflecting the action potential propagation in PFs, and a fEPSP reflecting mainly AMPA receptor-mediated PF to PC synaptic transmission (see Bergerot et al. (2013)). The fEPSP was reduced at 8 s following a burst of PF stimulation (10 pulses at 200 Hz). This transient depression has been named synaptically-evoked suppression of excitation (SSE). (B) The SSE was undetectable when the slice was superfused with 2 μM AM251. (C) Averaged SSE amplitude measured as a reduction of the integrated fEPSP ($fEPSP_{int}$) or the presynaptic calcium signal ($\Delta F/F$) ($n = 41$). AM251 abolished both responses similarly ($n = 10$). (D) SSE time course determined from $fEPSP_{int}$ monitoring. The SSE time course appeared slower than previously reported. The part of the SSE that recovered slowly was unaffected by 2 μM AM251. (E) Time course of the depression of presynaptic calcium signaling. The action potential-evoked transient increase in calcium concentration in PFs was monitored as $\Delta F/F$ signals. $\Delta F/F$ was depressed following the burst of ten pulses at 200 Hz (open symbols) or unaffected in the presence of 2 μM AM251 (filled symbols). (F) Superimposed time courses of the $\Delta F/F$ change shown in E (open symbols) and the CB1-dependent change in fEPSPs (CTL – AM: time course in AM (filled symbols in D) subtracted to the time course in CTR (open symbols in D)). The time course similarity suggests that the endocannabinoid-mediated reduction in presynaptic calcium signaling fully accounts for the CB1-mediated SSE.

Chan-Palay, 1974) where AMPA receptors account for most of the synaptic transmission (Konnerth et al., 1990; Farrant and Cull-Candy, 1991; Llano et al., 1991b). For the other boutons contacting stellate, basket and Golgi cells, a significant contribution of NMDA receptors to postsynaptic responses is expected. Since the fEPSP was not significantly affected by the NMDA receptor blocker D-AP5 at 50 μM (increased by 0.5 ± 1.6%, $n = 5$; $p = 0.77$), we conclude that the fEPSP satisfactorily provides specific monitoring of parallel fibers to Purkinje cell synaptic transmission.

In sagittal slices, eight seconds following a burst of ten pulses at 200 Hz, the fEPSP was reduced by 36.2 ± 3.5% ($n = 41$; $p = 7\,10^{-13}$; Fig. 4A,D). In AM251, a CB1 blocker, the fEPSP depression at +8 s following the burst was abolished ($p = 3\,10^{-6}$, $n = 10$; not significantly different from baseline: −1.6 ± 1.2%, $p = 0.22$, Fig. 4B, D), showing that the SSE monitored extracellularly at +8 s was all CB1-mediated (Fig. 4C). A small slower depression remained in AM251 (Fig. 4D), which is the correlate of a persistent posttetanic depression previously described and more prominent in older mice (Bergerot et al., 2013). The SSE could also be measured as the reduction in the double pulse-evoked presynaptic $[Ca^{2+}]_i$ rise. This latter method monitored endocannabinoid effects similarly (Fig. 4E): GCaMP2 $\Delta F/F$ was reduced by 34.0 ± 3.5% following the induction train ($n = 41$) and this effect was abolished in AM251 ($n = 10$, $p = 9\,10^{-8}$; Fig. 4C), consistent to previous reports using other calcium indicators (Brown et al., 2003) and confirming the presynaptic expression of SSE. The SSE of the fEPSP showed a longer time course than previously reported. Part of this longer time course was due to an additional short-term depression that remained in the presence of AM251 (Fig. 4D; Bergerot et al., 2013). This additional longer lasting depression was not due to a change in presynaptic action potential propagation which came back to the baseline very shortly following the induction train (not shown) and it was not reflected by a reduction of presynaptic $[Ca^{2+}]_i$ rise (Fig. 4E; Bergerot et al., 2013). Taking into account the small depression of the fEPSP that remained in AM251 (and thus, not CB1-mediated), the time course of the CB1-mediated SSE was similar when monitored as change in the fEPSP amplitude or in $\Delta F/F$ (Fig. 4F; expanded time scale for clarity).

Large variability in SSE potency

Surprisingly, despite recording extracellularly from a large population of synapses, the SSE potency was highly variable from one experiment to another (mean ± SD = 36.2 ± 24.4%; $n = 41$). In some cases, the SSE was merely detectable and only a slowly developing transient depression, similar to the one remaining in AM251 (Fig. 4D), was visible

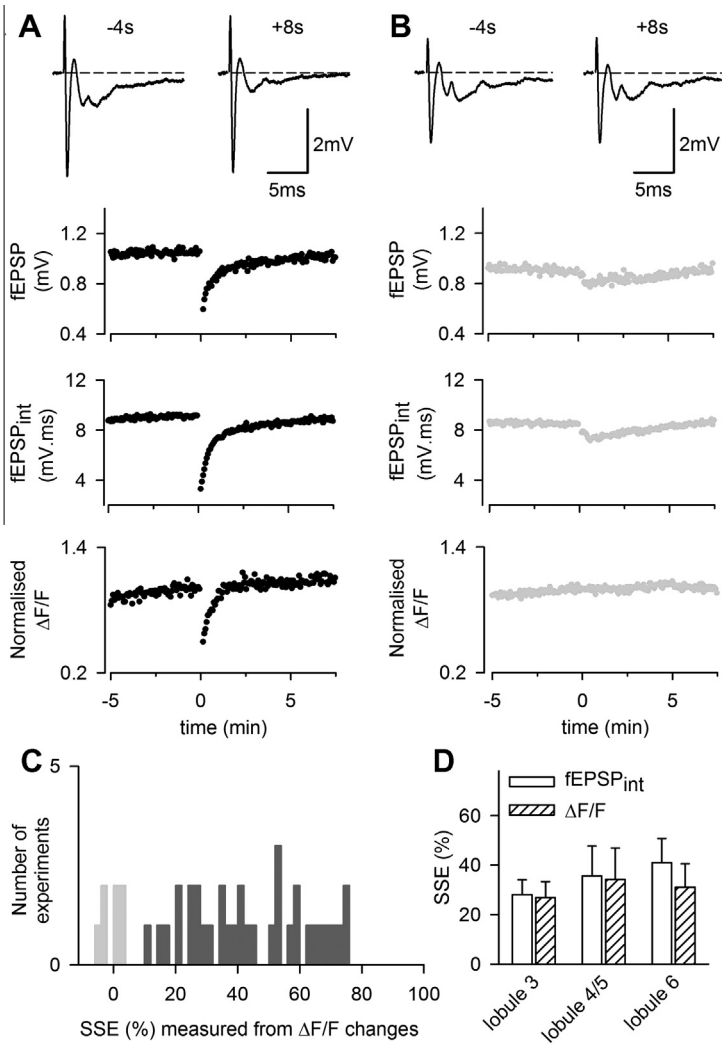

Fig. 5. SSE variability between sagittal slice preparations. (A) Example showing a ''typical SSE'', which can be measured as a depression of the fEPSP, the $fEPSP_{int}$ or the transient $[Ca^{2+}]_i$ rise in PFs. (B) Example showing an ''atypical SSE'', exhibiting a slower time-course and no detectable depression of presynaptic calcium signaling. (C) Distribution of experiments against the amplitude of the SSE quantified as the depression of $\Delta F/F$ change at +8 s following the induction (n = 41). (D) Comparison of the averaged SSE amplitude obtained for recording from lobules 3, 4/5 and 6 (n = 8, 6 and 6 respectively).

(Fig. 5B). In 15% of recordings, no transient depression of presynaptic calcium changes was detected (Fig. 5B, C). The effect of synaptically released glutamate on Purkinje cell mGluR1 activation and on endocannabinoid signaling has been reported to depend on EAAT4 expression level (Wadiche and Jahr, 2005) which is found to vary according to a sagittal pattern similar to that of zebrin II (aldolase C expression; Lehre et al., 1995). To assess whether our unreliability to observe SSE depended on this pattern of expression, we compared SSE amplitudes obtained from different lobules (3–6), lobule 3 having been reported to show the lowest EAAT4 expression (Wadiche and Jahr, 2005). As shown in Fig. 5D, the SSE was clearly not bigger in lobule 3 than in the other lobules, contrary to what would have been expected from the EAAT4 expression pattern. This indicates that EAAT4 expression does not account for the observed variability in SSE potency.

The effect of slice orientation on PF synaptic transmission and SSE

The variability in SSE might be caused by the variability in the slice quality. In order to assess this possibility, we compared two extreme opposite slice orientations: sagittal vs. transverse. Sagittal slicing is expected to be the most damageable for PFs, since all of them will be cut (their orientation being orthogonal to the slice orientation and their length largely exceeding the slice thickness). In contrast, transverse slices (in a plane parallel to PFs) are expected to preserve PFs best. We used on average the same stimulation intensity in both types of slices and obtained beams of stimulated PFs with similar section (Fig. 1I). In contrast to sagittal slices, the quantification of the number of activated PFs activated within a beam could hardly be derived from the $\Delta F/F$ signal produced by isolated single activated PFs. Indeed, in transverse slice, isolated PFs activated by GL stimulation produced

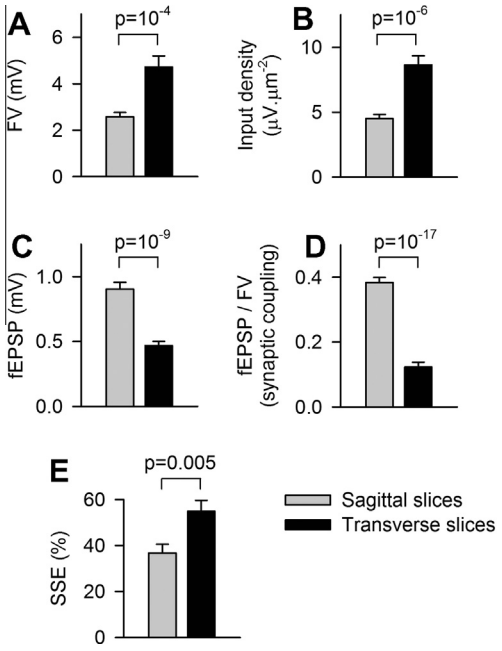

Fig. 6. Effect of slice orientations on input density, synaptic coupling and SSE. Sagittal (n = 41; gray) and transverse slices (n = 25; black) were compared. (A) The fiber volley (FV) was about twice bigger for recordings in transverse slices. (B) The input density (measured as the FV amplitude over the beam section) was twice bigger in transverse slices. (C) In contrast, the fEPSP was about half smaller in transverse slices. (D) As a result of (A) and (C), the synaptic coupling (defined as fEPSP/FV) was nearly 4 times smaller in transverse slices. (E) The amplitude of the SSE (measured as the change in $\Delta F/F$ signals, at +8 s following the induction) was significantly higher when recorded in transverse slices.

changes in GCaMP2 fluorescence which were less concentrated within the planar field of view and less detected above the background fluorescence. In order to compare the input density in sagittal and transverse slices, an input density index was defined as the FV amplitude (which increases with the number of activated PFs) over the beam section (an index of the volume occupied by the activated parallel fibers). As shown in Fig. 6A, B, the FV amplitude and the input density index were significantly larger in transverse slices than in sagittal slices (input density indexes were 8.6 ± 0.7 µV µm^{-2}, n = 25 and 4.5 ± 0.3 µV µm^{-2}, n = 41 respectively, $p = 10^{-5}$). By using the value $^{real}d_{PF}$ calculated from sagittal slices (Fig. 3I), we conclude that the average PF density in transverse slices is about 5.4 µm^{-2}.

In transverse slices, despite the doubling of the FV, the fEPSP was half smaller than in sagittal slices on average (Fig. 6C), suggesting that Purkinje cell preservation is four times reduced in transverse slices, presumably due to the truncation of their dendritic trees. This is illustrated by the synaptic coupling, calculated as the ratio of the fEPSP over the FV, showing that presynaptic activation was four-times less efficient at evoking a postsynaptic response in transverse slices compared to sagittal slices (Fig. 6D). This reduced postsynaptic activation could reflect either a decreased postsynaptic depolarization or a decrease in the number of Purkinje cells contributing to the extracellular field response. Both these cases might be expected to lead to reduced amount of endocannabinoid release. In the latter case, the reduced number of activated Purkinje cells could reduce the pooling of released endocannabinoids, which have been proposed to diffuse tens of µm before binding to CB1 receptors (Wilson and Nicoll, 2001). Thus, reduced postsynaptic activation should be associated to reduced SSE. However, we found that the SSE was significantly more potent in transverse slices (54.9 ± 4.8%) than in sagittal slices (36.2 ± 3.5%; p = 0.005, Fig. 6E). This finding suggests that the input density (which is higher in transverse slices) is more critical to enhance the SSE potency than the amount of postsynaptic activation.

Quantification of the SSE dependence on PF density

The widened SSE variability obtained by pooling the data from sagittal and transverse slices (Fig. 7A; SD = 25.7%; coefficient of variation, CV = 55%, n = 66) was used to maximize our chance to determine critical parameters correlating with the SSE potency. No significant correlation was detected between the SSE and the beam section diameter (Fig. 7B), indicating that the size of the dendritic area receiving converging inputs is not a crucial determinant of the SSE potency. The SSE correlated with the fEPSP amplitude when solely considering the data obtained from transverse slices (black symbols, Fig. 7C; $p = 10^{-5}$; n = 25). This correlation suggests that either Purkinje cell preservation favors the SSE occurrence (by pooling of endocannabinoids) or variable postsynaptic depolarization impacts on the SSE potency. However, over all the pooled data, the SSE did not significantly correlate with the fEPSP amplitude (p = 0.07; Fig. 7C), indicating that the amount of postsynaptic activation is not the only parameter that determines the SSE potency.

In contrast with these lacks of correlation, the SSE was loosely, but significantly correlated with the input density expressed as the FV over the section of the activated PF beam (p = 0.001, n = 66; 0D). Using our averaged estimate of $^{real}d_{PF}$ in sagittal slices (Fig. 3I) and assuming that the FV over the beam section is a fairly linear index of input density, we converted the input density scale into $^{real}d_{PF}$ units (Fig. 7D, top scale), i.e. the density of PFs which respond to the stimulation in the acute slice preparation. Fig. 2B suggests that a very low input density is obtained by granular layer stimulation (< 0.01 PF per µm^2). We have previously shown that no detectable SSE is evoked by such input (Marcaggi and Attwell, 2005), thus the plot of SSE against $^{real}d_{PF}$ was fitted by a simple exponential passing through the origin (no SSE for density < 0.01 µm^{-2}). This fit suggests that the maximum SSE obtained for high input density is 63% on average, and is more than half reduced for input densities lower than 1.9 µm^{-2}, i.e. a third of the averaged density we report here for transverse slices. In other words, the SSE is half reduced when the average separation between activated synapses is increased from ~1 to ~$3^{1/3}$ = 1.44 µm. The latter figure is based on the 0.93–0.98 µm^{-3} estimate for PF synapse density

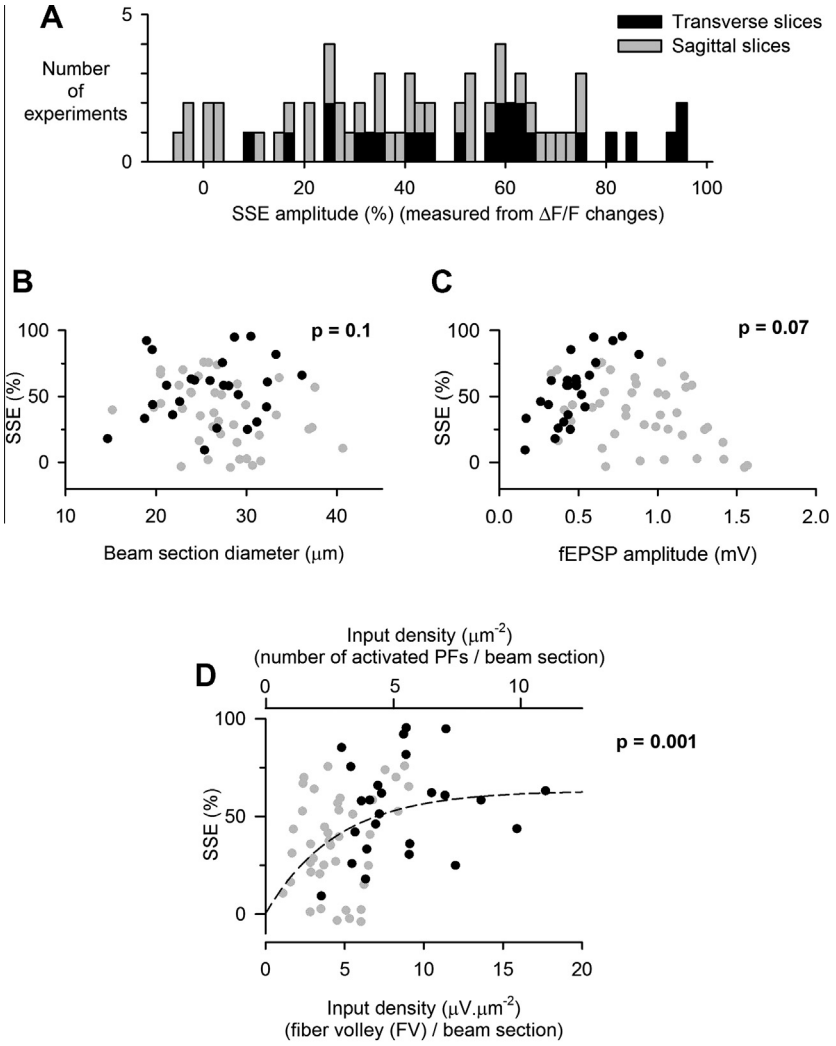

Fig. 7. Spearman rank order correlation between the SSE and the input density. (A) Data from recording from sagittal (gray; $n = 41$) and transverse (black; $n = 25$) slices are superimposed to extend the variabilty of SEE amplitude (determined from the change in $\Delta F/F$ at +8 s). (B) The SSE does not correlate significantly with the beam section diameter, which varied between experiments due to variations in the stimulation intensity. This shows that the SSE does not depend on the strength of the stimulation in the range explored. (C) The SSE plotted against the fEPSP amplitude exhibits a trend for a negative correlation, which does not reach statistical significance ($p = 0.07$). (D) The SSE showed a significant correlation with the input density index (FV amplitude divided by the beam section; in $\mu V\ \mu m^{-2}$). The input density unit was converted in number of PFs per surface unit of ML in the sagittal plane (μm^{-2}). An exponential regression of the data (passing through the origin since no SSE is detected for the very low input densities obtained with GL stimulation) is shown (dotted line).

obtained from quantitative analysis of electron micrographs of rat molecular layer (Napper and Harvey, 1988).

DISCUSSION

Central synapses have long been considered to operate independently from their neighbors, allowing information storage at individual synaptic boutons. Recently, however, the concept of spatially clustered plasticity has emerged: mechanisms of synaptic plasticity affecting clusters of synapses due to a biochemical compartmentalization of dendrites have been reported (Kleindienst et al., 2011; Makino and Malinow, 2011); clustered inputs have been imaged *in vivo* (Takahashi et al., 2012); and our previous data have shown that endocannabinoid-mediated plasticity depends on the spatial pattern of synapse activation (Marcaggi and Attwell, 2005). Here, we provide new data quantifying the spatial distribution of inputs required to induce endocannabinoid release.

The unique geometrical architecture of the cerebellar granule cell to Purkinje cell connectivity is expected to enable the experimental activation of strikingly different spatial patterns of inputs by stimulating granule cell axons either in the molecular layer or in the granular layer. Stimulations in the molecular layer or the granular layer are expected to activate clusters of synapses in close proximity or synapses sparsely scattered over the Purkinje cell dendritic tree, respectively (Fig. 2A, D). The difference between these spatial patterns has been assumed in previous studies (Marcaggi et al., 2003;

Marcaggi and Attwell, 2005, 2007). We now provide a direct visual confirmation of the striking difference between these spatial patterns by imaging parallel fiber activation in sagittal slices (Fig. 2B, E).

The synaptically-evoked endocannabinoid-mediated suppression of excitation (SSE) has been found to strikingly depend on these spatial patterns, since only observed for molecular layer stimulation (Marcaggi and Attwell, 2005, 2007). This result indicates that the convergence of inputs onto a same Purkinje cell dendritic region is required for SSE to occur. However, the data reported here indicate that the SSE can be undetectable despite the clustering of the inputs (molecular layer stimulation; Fig. 5B, C), unless the input density is sufficiently high (Fig. 7D). We conclude that endocannabinoid signaling does not only require the convergence of input onto a same dendritic domain, it also requires a high density of input that we have quantified. The SSE was not reliably observed unless the input densities was above $\sim 4\ \mu m^{-2}$ (Fig. 7D), i.e. close to its maximal average value of $6.07\ \mu m^{-2}$ estimated from anatomical data (Napper and Harvey, 1988). This tight dependency on the input density may underlie a homeostatic function of the endocannabinoid system: glutamate spillover-mediated synaptic crosstalk, which is enhanced when the input is dense (Marcaggi et al., 2003), is detected and downregulated by SSE (Marcaggi and Attwell, 2005). Our data support the hypothesis that the role of SSE is to reduce glutamate release when glutamate spillover-mediated synaptic crosstalk.

In conditions preventing the occurrence of the SSE (few pulses in the PF burst and low-stimulation intensity), (Brenowitz and Regehr, 2005) reported that a short-term depression could be rescued by pairing the PF burst with climbing fiber stimulation. This climbing fiber-assisted SSE is not to be confused with the SSE: the first is associative while the second is not, thus their roles may differ. Furthermore the mechanism of the climbing fiber-assisted SSE may be different, notably due to calcium dynamics specifically triggered by climbing fiber activation. Since these calcium dynamics appear to be prone to variability (Midtgaard et al., 1993), future studies should investigate the role of the climbing fiber-assisted SSE while quantitatively monitoring climbing fiber-evoked postsynaptic calcium changes.

The preservation of the synaptic density in acute superfused brain slices has remained unclear, especially when the axons carrying the presynaptic terminals are cut. We show that, in sagittal slices, the density of PFs which exhibit a detectable $[Ca^{2+}]_i$ rise in response to stimulation ($^{real}d_{PF}$) is $2.8\ \mu m^{-2}$, on average. Assuming that the density of PFs in intact tissue is approximately $6\ \mu m^{-2}$ (Napper and Harvey, 1988), or assuming that PFs are almost entirely preserved in transverse slices (where we find a twice higher density compared to sagittal slices, Fig. 6B), our data suggests that about 50% of PFs remain functional in sagittal slices. This is a high fraction considering that all the PFs are cut and less than 10% remain attached to their granule cell body (since the slice thickness is about one tenth of the average PF length (Soha et al., 1997)). We conclude that PFs are much better preserved in acute sagittal slices than may have been expected.

The width of the Purkinje cell dendritic tree (170–200 μm), the length of the parallel fibers (⩾2 mm) and their perpendicular arrangement make it impossible to preserve equally presynaptic and postsynaptic elements in a 200–300 μm slice (thickness above which proper oxygen supply from the superfusate to the core of the slice is compromised). Hence the best slicing orientation for studying the granule cell to Purkinje cell synapse has been debated: sagittal orientation being claimed to damage parallel fiber, while transverse orientation claimed to damage a large fraction of Purkinje cells due to truncation of their dendritic trees. Our data suggest that PFs are mostly preserved in transverse slices, and twice less in sagittal slices. Despite this higher preservation of PFs in transverse slices, the Purkinje cell response (fEPSP) is half reduced (Fig. 6C) compared to sagittal slices. Thus, our data suggest that, in sagittal slices, half the PFs are lost while four times more Purkinje cells survive. Overall, the tissue may be considered to be better preserved in sagittal slices than in transverse slices.

We found that the input density varied considerably from slice to slice preparations, irrespective of the method used for its calculation. The measurement of $^{real}d_{PF}$, based on the imaging of individual PFs, shows a coefficient of variation (CV) of 60% ($n = 11$; Fig. 3I). The measurement of the input density index (FV amplitude divided by the beam section) shows a CV of 45% ($n = 41$ sagittal slices; Fig. 7D). The latter measurement is more direct, supporting that the variability essentially reflects the variability in the preservation of PFs in acute slices rather than variability introduced by the calculation method. This variability is increased when input density indexes obtained from sagittal and transverse slices are pooled (CV = 55%, $n = 66$; Fig. 7D). This extended range of determined input densities was used to examine the link between SSE and input density. Although a significant correlation between SSE and input density is observed ($p = 0.001$) suggesting that part of the variability is accounted for by the variability in input density (Fig. 7D), this correlation is loose and the lack of correlation when considering data sets obtained for each slice orientation suggest that the SSE variability must also be accounted for by other factors, which yet remain to be determined. The exponential description of SSE dependence on input density suggests that the SSE is half reduced when the density drops from ~ 6 to $\sim 2\ \mu m^{-2}$, i.e. when the average distance between synapses increases from 1 to 1.44 μm. Thus the dependency of SSE on input density is for high-density values, when activated synapses are nearly adjacent. Does such input density occur in physiological conditions?

The physiological spatial pattern of PF to Purkinje cell inputs remains unknown. In rat, each Purkinje cell receives ~150,000 PF inputs (Napper and Harvey, 1988; Harvey and Napper, 1991). Paired granule cell/Purkinje cell recordings have provided an estimate of

the average synaptic strength of connections detected from the postsynaptic electric response recorded at the soma (Isope and Barbour, 2002). From this estimate, it has been proposed that about 150 such connections need to be simultaneously activated to reach the depolarization threshold required to evoke an action potential (Isope and Barbour, 2002). A large fraction of PF synapses has been reported to be silent (Ekerot and Jorntell, 2001; Isope and Barbour, 2002), this fraction has been estimated to be 85% (Isope and Barbour, 2002). Accordingly, 150/0.15 = 1000 parallel fiber synapses need to be recruited on average to activate 150 operating synapses and produce an action potential. This corresponds to 0.67% of the available input predicted from anatomical studies and an average input density of 0.04 μm^{-2}. According to our data, this input density is too low to mediate SSE. However, the input density is unlikely to be homogeneously distributed. If this input is spatially randomly distributed (Chen et al., 2011), the occurrence of two simultaneously activated synapses being adjacent will be more than 20 times per Purkinje cell, on average. Furthermore, recent data suggest that physiological input might produce clusters of activated PFs (Wilms and Hausser, 2010), the density of which remains to be determined. So clusters of dense inputs may occur in physiological conditions, either by chance (Chen et al., 2011) or as a result of compartmentalized correlated inputs (Takahashi et al., 2012).

Our finding supports our earlier proposal that the function of the SSE is homeostatic: it occurs when high glutamate spillover mediates synaptic crosstalk, and it downregulates synaptic crosstalk by reducing glutamate release. The optimization of the information storage capacity by independent operation of synapses is supported by modeling (Radulescu et al., 2009). We propose that the homeostatic downregulation of synaptic crosstalk by the endocannabinoid system, by promoting independent operation of neighboring synapses, maximizes the information storage capacity of the cerebellum (Marcaggi and Attwell, 2005).

Acknowledgments—This work was supported by the Career Development Award G0600064 from the United Kingdom Medical Research Council to PM. We thank Marco Beato for giving us access to his confocal microscope.

REFERENCES

Beierlein M, Gee KR, Martin VV, Regehr WG (2004) Presynaptic calcium measurements at physiological temperatures using a new class of dextran-conjugated indicators. J Neurophysiol 92:591–599.

Bergerot A, Rigby M, Bouvier G, Marcaggi P (2013) Persistent posttetanic depression at cerebellar parallel fiber to Purkinje cell synapses. PLoS One 8:e70277.

Brenowitz SD, Regehr WG (2005) Associative short-term synaptic plasticity mediated by endocannabinoids. Neuron 45:419–431.

Brown SP, Brenowitz SD, Regehr WG (2003) Brief presynaptic bursts evoke synapse-specific retrograde inhibition mediated by endogenous cannabinoids. Nat Neurosci 6:1048–1057.

Brown SP, Safo PK, Regehr WG (2004) Endocannabinoids inhibit transmission at granule cell to Purkinje cell synapses by modulating three types of presynaptic calcium channels. J Neurosci 24:5623–5631.

Chen X, Leischner U, Rochefort NL, Nelken I, Konnerth A (2011) Functional mapping of single spines in cortical neurons in vivo. Nature 475:501–505.

Chevaleyre V, Takahashi KA, Castillo PE (2006) Endocannabinoid-mediated synaptic plasticity in the CNS. Annu Rev Neurosci 29:37–76.

Daniel H, Crepel F (2001) Control of Ca(2+) influx by cannabinoid and metabotropic glutamate receptors in rat cerebellar cortex requires K(+) channels. J Physiol 537:793–800.

Daniel H, Rancillac A, Crepel F (2004) Mechanisms underlying cannabinoid inhibition of presynaptic Ca^{2+} influx at parallel fibre synapses of the rat cerebellum. J Physiol 557:159–174.

Diez-Garcia J, Matsushita S, Mutoh H, Nakai J, Ohkura M, Yokoyama J, Dimitrov D, Knopfel T (2005) Activation of cerebellar parallel fibers monitored in transgenic mice expressing a fluorescent Ca^{2+} indicator protein. Eur J Neurosci 22:627–635.

Dugue GP, Dumoulin A, Triller A, Dieudonne S (2005) Target-dependent use of co-released inhibitory transmitters at central synapses. J Neurosci 25:6490–6498.

Ekerot CF, Jorntell H (2001) Parallel fibre receptive fields of Purkinje cells and interneurons are climbing fibre-specific. Eur J Neurosci 13:1303–1310.

Farrant M, Cull-Candy SG (1991) Excitatory amino acid receptor-channels in Purkinje cells in thin cerebellar slices. Proc Biol Sci 244:179–184.

Harvey RJ, Napper RM (1991) Quantitative studies on the mammalian cerebellum. Prog Neurobiol 36:437–463.

Heifets BD, Castillo PE (2009) Endocannabinoid signaling and long-term synaptic plasticity. Annu Rev Physiol 71:283–306.

Isope P, Barbour B (2002) Properties of unitary granule cell → Purkinje cell synapses in adult rat cerebellar slices. J Neurosci 22:9668-9678.

Kano M, Ohno-Shosaku T, Hashimotodani Y, Uchigashima M, Watanabe M (2009) Endocannabinoid-mediated control of synaptic transmission. Physiol Rev 89:309–380.

Kleindienst T, Winnubst J, Roth-Alpermann C, Bonhoeffer T, Lohmann C (2011) Activity-dependent clustering of functional synaptic inputs on developing hippocampal dendrites. Neuron 72:1012–1024.

Konnerth A, Llano I, Armstrong CM (1990) Synaptic currents in cerebellar Purkinje cells. Proc Natl Acad Sci USA 87:2662–2665.

Kreitzer AC, Regehr WG (2001) Retrograde inhibition of presynaptic calcium influx by endogenous cannabinoids at excitatory synapses onto Purkinje cells. Neuron 29:717–727.

Lehre KP, Levy LM, Ottersen OP, Storm-Mathisen J, Danbolt NC (1995) Differential expression of two glial glutamate transporters in the rat brain: quantitative and immunocytochemical observations. J Neurosci 15:1835–1853.

Llano I, Leresche N, Marty A (1991a) Calcium entry increases the sensitivity of cerebellar Purkinje cells to applied GABA and decreases inhibitory synaptic currents. Neuron 6:565–574.

Llano I, Marty A, Armstrong CM, Konnerth A (1991b) Synaptic- and agonist-induced excitatory currents of Purkinje cells in rat cerebellar slices. J Physiol 434:183–213.

Makino H, Malinow R (2011) Compartmentalized versus global synaptic plasticity on dendrites controlled by experience. Neuron 72:1001–1011.

Marcaggi P, Attwell D (2005) Endocannabinoid signaling depends on the spatial pattern of synapse activation. Nat Neurosci 8:776–781.

Marcaggi P, Attwell D (2007) Short- and long-term depression of rat cerebellar parallel fibre synaptic transmission mediated by synaptic crosstalk. J Physiol 578:545–550.

Marcaggi P, Billups D, Attwell D (2003) The role of glial glutamate transporters in maintaining the independent operation of juvenile mouse cerebellar parallel fibre synapses. J Physiol 552:89–107.

Midtgaard J, Lasser-Ross N, Ross WN (1993) Spatial distribution of Ca^{2+} influx in turtle Purkinje cell dendrites in vitro: role of a transient outward current. J Neurophysiol 70:2455–2469.
Mintz IM, Sabatini BL, Regehr WG (1995) Calcium control of transmitter release at a cerebellar synapse. Neuron 15:675–688.
Napper RM, Harvey RJ (1988) Number of parallel fiber synapses on an individual Purkinje cell in the cerebellum of the rat. J Comp Neurol 274:168–177.
Ohno-Shosaku T, Maejima T, Kano M (2001) Endogenous cannabinoids mediate retrograde signals from depolarized postsynaptic neurons to presynaptic terminals. Neuron 29:729–738.
Palay S, Chan-Palay V (1974) Cerebral cortex. New York: Springer.
Palkovits M, Magyar P, Szentagothai J (1971) Quantitative histological analysis of the cerebellar cortex in the cat. 3. Structural organization of the molecular layer. Brain Res 34:1–18.
Pichitpornchai C, Rawson JA, Rees S (1994) Morphology of parallel fibres in the cerebellar cortex of the rat: an experimental light and electron microscopic study with biocytin. J Comp Neurol 342:206–220.
Radulescu A, Cox K, Adams P (2009) Hebbian errors in learning: an analysis using the Oja model. J Theor Biol 258:489–501.
Safo PK, Cravatt BF, Regehr WG (2006) Retrograde endocannabinoid signaling in the cerebellar cortex. Cerebellum 5:134–145.
Safo PK, Regehr WG (2005) Endocannabinoids control the induction of cerebellar LTD. Neuron 48:647–659.
Soha JM, Kim S, Crandall JE, Vogel MW (1997) Rapid growth of parallel fibers in the cerebella of normal and staggerer mutant mice. J Comp Neurol 389:642–654.
Takahashi N, Kitamura K, Matsuo N, Mayford M, Kano M, Matsuki N, Ikegaya Y (2012) Locally synchronized synaptic inputs. Science 335:353–356.
Tanimura A, Yamazaki M, Hashimotodani Y, Uchigashima M, Kawata S, Abe M, Kita Y, Hashimoto K, Shimizu T, Watanabe M, Sakimura K, Kano M (2010) The endocannabinoid 2-arachidonoylglycerol produced by diacylglycerol lipase alpha mediates retrograde suppression of synaptic transmission. Neuron 65:320–327.
Wadiche JI, Jahr CE (2005) Patterned expression of Purkinje cell glutamate transporters controls synaptic plasticity. Nat Neurosci 8:1329–1334.
Wilms CD, Hausser M (2010) Spatially clustered activation of cerebellar parallel fibers by sensory stimuli. In: FENS, p 141.120 Amsterdam.
Wilson RI, Nicoll RA (2001) Endogenous cannabinoids mediate retrograde signalling at hippocampal synapses. Nature 410:588–592.
Xu-Friedman MA, Harris KM, Regehr WG (2001) Three-dimensional comparison of ultrastructural characteristics at depressing and facilitating synapses onto cerebellar Purkinje cells. J Neurosci 21:6666–6672.

(Accepted 22 October 2013)
(Available online 30 October 2013)